

Simultaneous Map and Object Reconstruction

Nathaniel Chodosh¹, Anish Madan¹, Deva Ramanan¹, and Simon Lucey²

¹ Carnegie Mellon University {nchodosh, anishmad, deva}@cs.cmu.edu

² University of Adelaide
simon.lucey@adelaide.edu.au

Abstract. In this paper, we present a method for dynamic surface reconstruction of large-scale urban scenes from LiDAR. Depth-based reconstructions tend to focus on small-scale objects or large-scale SLAM reconstructions that treat moving objects as outliers. We take a holistic perspective and optimize a compositional model of a dynamic scene that decomposes the world into rigidly moving objects and the background. To achieve this, we take inspiration from recent novel view synthesis methods and pose the reconstruction problem as a global optimization, minimizing the distance between our predicted surface and the input LiDAR scans. We show how this global optimization can be decomposed into registration and surface reconstruction steps, which are handled well by off-the-shelf methods without any re-training. By careful modeling of continuous-time motion, our reconstructions can compensate for the rolling shutter effects of rotating LiDAR sensors. This allows for the first system (to our knowledge) that properly motion compensates LiDAR scans for rigidly-moving objects, complementing widely-used techniques for motion compensation of static scenes. Beyond pursuing dynamic reconstruction as a goal in and of itself, we also show that such a system can be used to auto-label partially annotated sequences and produce ground truth annotation for hard-to-label problems such as depth completion and scene flow.

1 Introduction

Dynamic scene understanding aims to produce a model of the world that explains all measurements over time. In the context of depth sensors, this problem is posed as dynamic surface reconstruction, where the goal is to produce a time-varying surface that matches a sequence of depth measurements. This problem has been widely studied in the context of handheld RGB-D sensors capturing human-scale scenes [18, 22, 33, 37]. However, investment in autonomous driving has created a new mode of depth capture — spinning LiDAR sensors atop moving vehicles — which is largely unaddressed by the existing research. Existing methods focus on reconstructing a few densely-scanned non-rigid objects, but autonomous driving scenes are typically composed of many sparsely-scanned rigid objects [4, 7]. In this work, we propose the first dynamic surface reconstruction system aimed

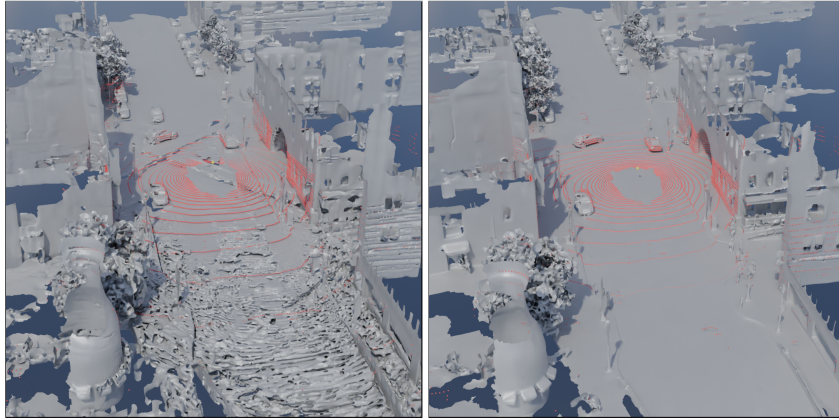


Fig. 1: Surface reconstruction of a dynamic sequence from NuScenes. Given ego-pose and bounding box annotations, a naive approach would aggregate background and object points into common reference frames and then run a point-to-surface reconstruction algorithm. Even human annotations are not accurate enough for this simple approach (**top left**). Instead, we design an optimization that refines both the ego and object poses, yielding high-quality reconstructions (**top right**). The input LiDAR sweep is plotted with red and blue spheres, red for background points and blue for dynamic. The naive approach also fails due to rolling shutter effects on fast-moving vehicles (see Fig. 2)

at operating in this setting. In addition to producing compelling visual results, our system is able to **substantially improve the quality of ground truth annotations** of ego-vehicle pose and object tracks provided in flagship datasets such as NuScenes [3] and Argoverse [32].

Approach: We address the dynamic scene reconstruction problem from a classic “analysis by synthesis” perspective; we synthesize a dense spacetime reconstruction via a compositional model of geometry and motion. We then measure the 3D error of the reconstruction with respect to the observed LiDAR scans. Finally, we optimize the geometry and motion to minimize this 3D error. We take care to formulate the optimization so that it can be efficiently decomposed into alternating steps of 1) estimating 6-DOF motion parameters of rigidly-moving components (including the moving ego-vehicle) and 2) estimating the geometry of each rigid component (including the static background). Such a decomposition allows us to leverage off-the-shelf solutions to the point registration and point-to-mesh surface reconstruction problems, respectively. Interestingly, by modeling 6-DOF pose trajectories continuously, our reconstructions can easily account for the “rolling shutter” effects of rotating LiDAR scanners. This allows our reconstructions to properly motion-compensate LiDAR scans for moving objects (for the first time, to our knowledge), complementing widely-used techniques for motion-compensation of static scenes (see Fig. 2).

Applications: Our goal is to generate dynamic scene reconstructions that provide high-quality annotations for downstream autonomous driving tasks. Labeling in-the-wild data is extremely costly, and as a result, many autonomous

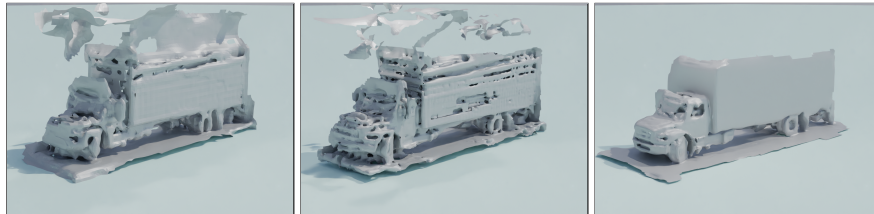


Fig. 2: Accurate object poses and accounting for intra-sweep motion are critical for high-quality reconstructions. The **(Left)** column shows the reconstruction with neither refined poses nor object-motion compensation, the **(middle)** column shows the reconstruction with refined poses but without object-motion compensation, and the **(right)** column shows the result of combining both.

driving tasks rely on re-processing existing data of varying quality. For example, depth completion benchmarks use aggregated LiDAR sweeps to generate ground truth “dense” depth reconstructions [26]. This results in annotated data with well-documented occlusion errors and motion artifacts that are nonetheless still used for training and evaluation [31, 38]. An example of the depth maps produced by our method is shown in Fig. 3. Scene flow is another autonomous driving task that re-processes existing AV datasets, using annotated bounding box motion between frames as a proxy for the underlying ground-truth motion field [1, 14], which also has well-documented issues in evaluation [4]. Accurate time-space reconstructions of the rigidly moving objects in the scene are critical to both of these tasks. We demonstrate that the ground-truth motion annotations are insufficient for producing these reconstructions and that our system significantly improves upon them. We provide numerous qualitative visuals that speak to our accuracy (including those in the supplement), but providing quantitative results is challenging since we often outperform the ground truth to which one normally compares! That said, we do provide quantitative metrics such as point-to-surface error metrics. Moreover, we show that our dynamic reconstruction engine can already be used as a practical system for fully or semi-automatic annotation by converting the output of off-the-shelf object trackers or low-frame rate human annotations into high-frame rate reconstructions. In particular, we outperform the baseline approach of linear-interpolated annotations, which is widely-used despite its simplicity [1, 4, 14].

In short, our main contributions are posing the classic dynamic surface reconstruction problem in a new setting, proposing new downstream applications of this problem, and demonstrating a simple yet effective optimization-based solution.

2 Related Work

Dynamic Surface Reconstruction: Reconstruction of non-rigid surfaces from depth scanners has been studied for over two decades [17]. Early work overcame

the inherent ill-posedness of the problem by relying on object-specific shape models for humans [23], faces [13] and hands [21]. Since then, many works have demonstrated template-free reconstruction in both the online [18] and offline settings [19]. This line of work is focused on highly deformable objects such as people and animals, which are very close to the depth sensor. As a result, they do not apply to the long-range, generally rigid world of autonomous driving scenes.

Dynamic SLAM: Since we are solving for the global map of the world as well as the sensor’s location within it, our work is closely related to SLAM in general and specifically to Dynamic SLAM, sometimes called SLOT (Simultaneous Localization and Object Tracking). Many works identify dynamic objects to remove them from the global map [8], but some track dynamic objects and register new observations to an object template. Similar to our work, these approaches typically represent the world as a composition of rigid bodies [2, 6, 9, 24, 29, 34]. These methods are focused on real-time operation from RGB inputs rather than offline LiDAR processing. As a result, they generally do not reconstruct detailed surface representations of the tracked objects, although that has been proposed as a post-processing step to the tracked objects [11]. Also similar to our work are SLAM methods, which create a dense surface reconstruction of the global map [13, 27]. However, to our knowledge, none of these approaches reconstruct dynamic objects.

Asset Generation for Autonomous Driving: Related to the object reconstruction component of our system is the line of work focused on creating high-quality mesh reconstructions of vehicles for simulation purposes [15, 30, 35]. These methods are similar to ours in that they reconstruct dense meshes of in-the-wild vehicles but have several key differences. First, since these systems aim to extract assets, not reconstruct complete sequences, they focus on objects that are close to the sensor and have accurate poses from object detection. Although this is not made explicit, the result is that these systems are made to operate on stationary objects, not dynamic ones. Second, they rely heavily on RGB information as well as depth sensors. As we show, reconstructing moving objects from spinning LiDARs requires careful handling of the rolling-shutter effect. This makes it challenging to incorporate global-shutter RGB cameras. The fact that these works make no mention of this further indicates that they do not handle dynamic objects.

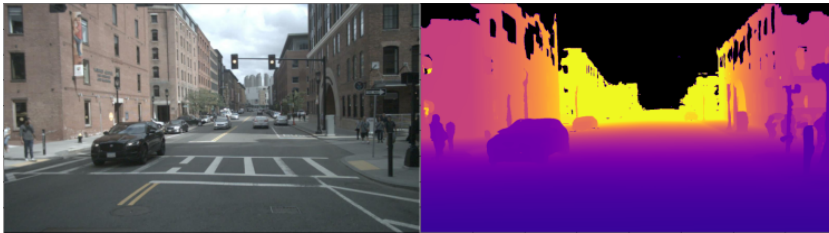


Fig. 3: An example dense depth map produced by our method

3 Problem Statement

We assume as input a sequence of LiDAR sweeps measured at timestamps $t \in \mathcal{T}$, and coarse tracks of K objects. Since we are using a compositional model of the scene, we will need a coordinate frame for each component.

- **Ego coordinates:** This is the coordinate frame that the input points are measured in. That is, the coordinate frame where the LiDAR sensor is at the origin and the z-direction points along the rotation axis. Since the ego-vehicle is moving, this coordinate frame changes over time. We will denote the sensor coordinate frame at time t as e_t .
- **Object coordinates:** To each of the K objects in the sequence, we will assign a coordinate system where the object is at the origin, the z-direction is up and the x-direction is “forward”. Each of these coordinate systems also varies with time to express the dynamic object motion. We will denote the i th object’s coordinate frame at time t as o_t^i .
- **World coordinates:** This is the fixed global coordinate frame of the scene, which we denote as w .

Importantly, we represent the static background in this fixed world coordinate frame. Due to the global coordinate frame ambiguity, we will choose this frame to be equal to e_1 .

To indicate the coordinate frame of given point \mathbf{x} , or set of points \mathbf{X} we will use subscripts: for example, we write input points as \mathbf{x}_{e_t} , \mathbf{X}_{e_t} . We will express the relationships between these coordinate frames using 4×4 rigid transformation matrices \mathbf{T} . We write the transformation from world coordinates at time t to sensor coordinates e_t as $\mathbf{T}_w^{e_t}$. Similarly, the transformation from object i at time t to world coordinates is written as $\mathbf{T}_{o_t^i}^w$. Then, transformation from the i th object’s coordinate system at time t to the sensor coordinates at time t can be written as $\mathbf{T}_{o_t^i}^{e_t} = \mathbf{T}_w^{e_t} \mathbf{T}_{o_t^i}^w$.

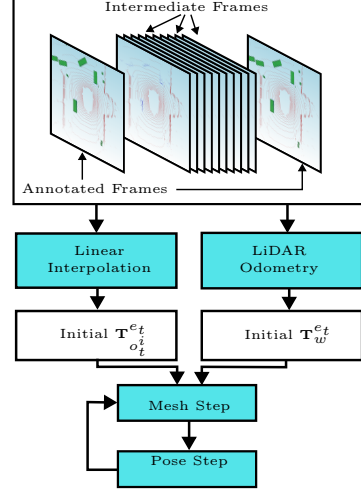


Fig. 4: A high-level overview of our method when used with sparse ground truth annotations. We take the annotated LiDAR frames that make use of interpolation and off-the-shelf LiDAR odometry to initialize object and ego poses for all frames. Our global optimization makes use of coordinate descent to update the geometry and motion alternately. When using the output of an object tracker as input, we omit the interpolation step, as the tracks cover all the input frames.

We aim to decompose the scene into a set of surfaces that transform rigidly over time. Our approach is agnostic to the particular choice of surface representation, but we use triangular meshes since they are lightweight and widely used. We will have a mesh for each of the K objects in the scene $\{\mathcal{M}_i\}_{i=1}^K$ as well as the background \mathcal{M}_0 . In a slight abuse of notation, we will write $\mathbf{T}\mathcal{M}$ to denote transforming the vertices of \mathcal{M} by the transformation \mathbf{T} . Similarly, we will write $\mathbf{T}\mathbf{X}$ to express transforming the points \mathbf{X} . The union of two meshes will be written as $[\mathcal{M}_1, \mathcal{M}_2]$. Finally, we will measure the 3D distance between a mesh and a point cloud using the nearest neighbor loss

$$\mathcal{D}(\mathcal{M}, \mathbf{X}) = \sum_{\mathbf{x} \in \mathbf{X}} \min_{\mathbf{m} \in \mathcal{M}} \|\mathbf{m} - \mathbf{x}\|. \quad (1)$$

4 Objective

We aim to find surfaces and their 6-DOF motion parameters such that their composition matches the measured pointcloud at each timestep. Since our pointclouds are measured in the ego coordinates e_t , we must transform our meshes into that frame. Consider a scene composed of a background mesh (\mathcal{M}_0) and a single object (\mathcal{M}_1). To transform object \mathcal{M}_1 into e_t , we first place it in the world via $\mathbf{T}_{o_1}^w$ and then view the world from the sensor frame via $\mathbf{T}_w^{e_t}$. We can use the transformation $\mathbf{T}_{o_1}^{e_t} = \mathbf{T}_w^{e_t} \mathbf{T}_{o_1}^w$ to accomplish both. To transform the static background mesh (which is already represented in world coordinates), we need only transform it by $\mathbf{T}_w^{e_t}$. Once all surfaces have been transformed into frame e_t , the composite reconstruction $[\mathbf{T}_w^{e_t} \mathcal{M}_0, \mathbf{T}_{o_1}^{e_t} \mathcal{M}_1]$ is compared to the measured LiDAR points \mathbf{X}_{e_t} using the nearest-neighbor distance from Eq. (1). Summing this over all time produces our final reconstruction error:

$$\min_{\{\mathcal{M}_i, \mathbf{T}_{o_i}^{e_t}, \mathbf{T}_w^{e_t}\}} \sum_{t \in \mathcal{T}} \mathcal{D}([\mathbf{T}_w^{e_t} \mathcal{M}_0, \mathbf{T}_{o_1}^{e_t} \mathcal{M}_1, \dots, \mathbf{T}_{o_K}^{e_t} \mathcal{M}_K], \mathbf{X}_{e_t}). \quad (2)$$

4.1 Decomposition

We could use a differentiable renderer and optimize Eq. (2) with gradient descent. But, we will demonstrate that decomposing the optimization into discrete sub-components allows us to leverage off-the-shelf tools and yields good reconstructions. To aid in this decomposition, let $\mathbf{X}_{e_t}^i$ denote the subset of points from \mathbf{X}_{e_t} which fall on object i . This assignment can be coarse, and in practice, we assign points to the bounding box they fall into and to the background if they are not contained in any bounding box. Once we have refined the poses of the bounding boxes, we can recompute this step to get new assignments. Using this notation, we can further break down Eq. (2) into:

$$\min_{\{\mathcal{M}_i, \mathbf{T}_{o_i}^{e_t}, \mathbf{T}_w^{e_t}\}} \sum_{t \in \mathcal{T}} \sum_{i=0}^K \mathcal{D}(\mathbf{T}_{o_i}^{e_t} \mathcal{M}_i, \mathbf{X}_{e_t}^i), \quad (3)$$

where we let $o_t^0 = w$ for notional simplicity.

Our approach consists of applying coordinate descent: alternating between fixing the poses to optimize the meshes and then fixing the meshes to update the poses. These stages are the **pose step** and **mesh step**, respectively. The coarse bounding boxes are used to initialize $\mathbf{T}_{o_t^i}^{e_t}$ and an off-the-shelf LiDAR odometry method is used to initialize $\mathbf{T}_w^{e_t}$. We do not require any initialization of the meshes. A schematic of the pipeline is shown in Fig. 4.

4.2 Mesh Step

Assuming fixed poses, we can estimate new meshes by solving

$$\mathcal{M}_i \leftarrow \arg \min_{\mathcal{M}_i} \sum_{t \in \mathcal{T}} \mathcal{D}(\mathbf{T}_{o_t^i}^{e_t} \mathcal{M}_i, \mathbf{X}_{e_t}^i). \quad (4)$$

We can make use of two identities related to the nearest neighbor distance to transform this optimization into a well-known problem. First, we can use the fact the distance is unaffected by a global rigid transformation to see that $\mathcal{D}(\mathbf{T}\mathcal{M}, \mathbf{X}) = \mathcal{D}(\mathcal{M}, \mathbf{T}^{-1}\mathbf{X})$. Second, if we write a set of points $\mathbf{X} = [\mathbf{X}_1, \mathbf{X}_2]$ as a union of two disjoint sets \mathbf{X}_1 and \mathbf{X}_2 , we can see that $\mathcal{D}(\mathcal{M}, [\mathbf{X}_1, \mathbf{X}_2]) = \mathcal{D}(\mathcal{M}, \mathbf{X}_1) + \mathcal{D}(\mathcal{M}, \mathbf{X}_2)$. Now we combine them to get:

$$\begin{aligned} \mathcal{M}_i &\leftarrow \arg \min_{\mathcal{M}_i} \sum_{t \in \mathcal{T}} \mathcal{D}(\mathbf{T}_{o_t^i}^{e_t} \mathcal{M}_i, \mathbf{X}_{e_t}^i) \\ &= \arg \min_{\mathcal{M}_i} \sum_{t \in \mathcal{T}} \mathcal{D}(\mathcal{M}_i, (\mathbf{T}_{o_t^i}^{e_t})^{-1} \mathbf{X}_{e_t}^i) \\ &= \arg \min_{\mathcal{M}_i} \mathcal{D} \left(\mathcal{M}_i, \left[(\mathbf{T}_{o_t^i}^{e_t})^{-1} \mathbf{X}_{e_t}^i, \dots \right] \right). \end{aligned} \quad (5)$$

The final form of this equation can be interpreted as a standard static point-to-surface reconstruction problem. We use the recent Neural Kernel Surface Reconstruction [10], but any technique, such as Poisson surface reconstruction [12], could be used.

4.3 Pose Step

Assuming fixed meshes, we can estimate new poses by solving

$$\begin{aligned} \mathbf{T}_{o_t^i}^{e_t} &\leftarrow \arg \min_{\mathbf{T}_{o_t^i}^{e_t}} \mathcal{D} \left(\mathbf{T}_{o_t^i}^{e_t} \mathcal{M}_i, \mathbf{X}_{e_t}^i \right) \\ &= \arg \min_{\mathbf{T}_{o_t^i}^{e_t}} \mathcal{D} \left(\mathcal{M}_i, (\mathbf{T}_{o_t^i}^{e_t})^{-1} \mathbf{X}_{e_t}^i \right). \end{aligned} \quad (6)$$

This is a point-to-mesh registration problem that is well-studied under the family of Iterative Closest Point (ICP) methods. However, there is a complication that we thus far have avoided by being vague about the definition of a LiDAR sweep.

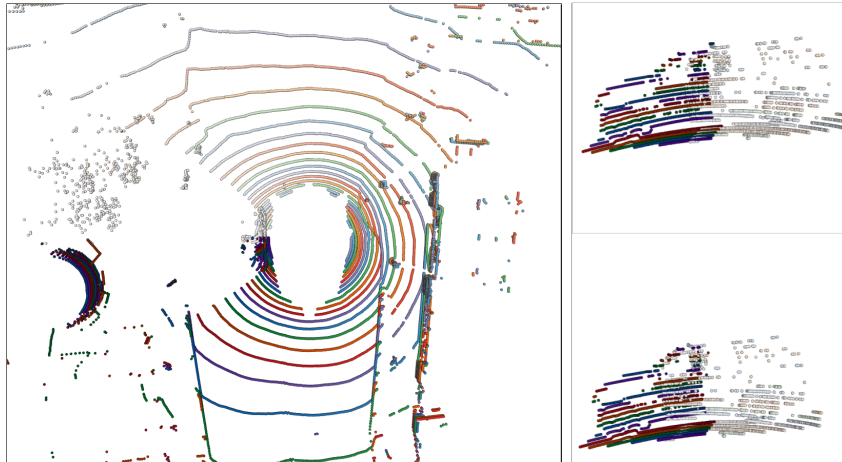


Fig. 5: (Left) A LiDAR sweep where each point has been colored according to which laser it belongs to (hue) and the time within the sweep it was acquired (lighter is earlier, darker is later). A moving car is passing the ego-vehicle on the left and is captured at both the start and end of the sweep (**top right**), leading to distortion (the driver-side window is captured twice in different locations). Accounting for this distortion by modeling the object motion is key to the quality of our reconstructions (**bottom right**).

4.4 What *is* a LiDAR sweep?

Revolving LiDAR sensors do not have a global shutter. Instead, they rotate continuously and measure depth across 16-128 vertically arranged lasers, typically taking 100ms to complete a 360-degree rotation. Depth along each laser ray is measured with respect to the (potentially moving) ego sensor frame (see Fig. 6). Most software packages abstract away this continuous capture and instead generate a *virtual* sweep of point measurements that would have been obtained if the sensor captured the world a single time instant with a global 360-degree shutter. To do so, robotic platforms typically transform all points to a chosen reference frame (by exploiting knowledge of continuous ego pose during the 100ms capture window, often obtained with a constant velocity assumption).

Such motion compensation will generate the correct virtual point cloud for a static world but will **not** correctly compensate for moving objects in a dynamic world. This well-known phenomenon is often manifested as vertical “seams” that appear in a sweep since points on either side of the seam are collected 100ms apart (Fig. 5). However, our spacetime optimization can correctly model moving objects by letting our time index t be a continuous variable rather than an integer frame index. For example, if we have a 16-beam LiDAR sensor that takes 1080 measurements in a single rotation, the first 16 points of our sequence are written as $\mathbf{X}_{e_{1/1080}}$. Importantly, our global optimization Eq. (2), mesh step Eq. (4), and pose step Eq. (6) are just as valid under this interpretation of a sweep “slice”, but with 1080 times as many poses. This is computationally expensive and may underconstrain the optimization. To avoid this, we adopt a constant velocity model for poses between “keyframes” placed at the end of every complete sensor

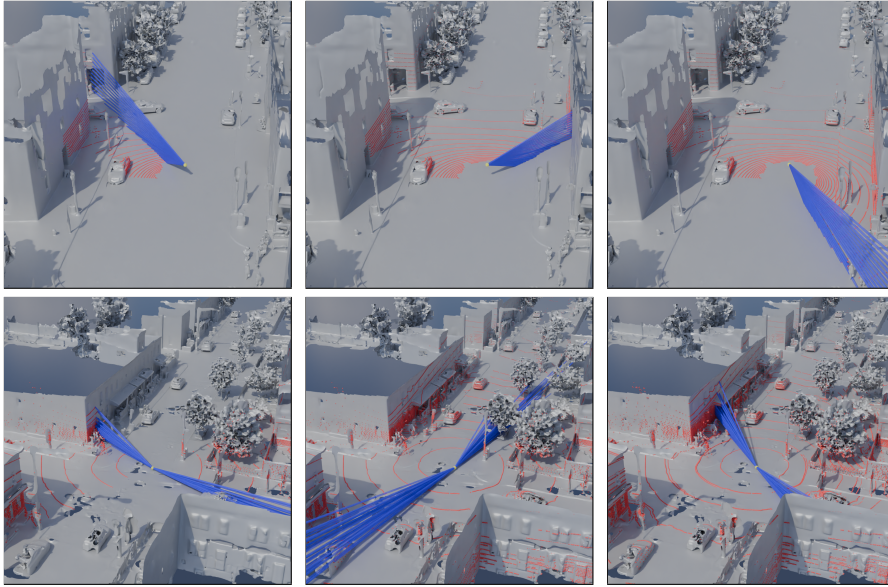


Fig. 6: LiDAR returns are often grouped and processed in 360-degree sweeps, but most sensors have a continuous “shutter” as they rotate. Our framework can model this continuous shutter for any combination of LiDAR sensors or scanning patterns. We find that this modeling has a large impact on the quality of reconstructed objects. Here, we visualize the set of points within a sweep, which are captured simultaneously (green lines) for NuScenes (**top**) and Argoverse (**bottom**). Argoverse has two LiDAR sensors spinning 180 degrees out of phase, leading to two sets of points being captured at each instant.

rotation. For example, we can express the continuous pose of the sensor for $0 < t < 1$ using the keyframe poses $\mathbf{T}_{e_0}^w, \mathbf{T}_{e_1}^w$ like so:

$$\begin{aligned} \mathbf{T}_w^{e_1} (\mathbf{T}_w^{e_0})^{-1} &= \begin{bmatrix} \mathbf{R}_{3 \times 3} & \mathbf{v}_{3 \times 1} \\ \mathbf{0}_{1 \times 3} & 1 \end{bmatrix}, \quad \mathbf{w} = \log(\mathbf{R}) \\ \mathbf{T}_{e_t}^w &= \mathbf{T}_{e_1}^w \begin{bmatrix} e^{\mathbf{w}(1-t)} & \mathbf{v}(1-t) \\ \mathbf{0}_{1 \times 3} & 1 \end{bmatrix} = \mathbf{T}_{e_1}^w \mathbf{T}_{e_t}^{e_1}. \end{aligned} \quad (7)$$

Just as we assumed that the ego-vehicle obeys a constant velocity model between keyframes, we can make the same assumption about the motion of other objects in the scene. However, care needs to be taken to ensure that the constant velocity assumption is applied to the object’s motion *with respect to the world* as opposed to with respect to the ego-vehicle. Constant velocity in the world frame is not equivalent to constant velocity in the moving sensor frame due to the presence of rotations. With this in mind, we represent the object

poses like so:

$$\begin{aligned} (\mathbf{T}_{e_1}^{o_1} \mathbf{T}_w^{e_1}) (\mathbf{T}_{e_0}^{o_0} \mathbf{T}_w^{e_0})^{-1} &= \begin{bmatrix} \mathbf{R}_{3 \times 3} & \mathbf{v}_{3 \times 1} \\ \mathbf{0}_{1 \times 3} & 1 \end{bmatrix}, \quad \mathbf{w} = \log(\mathbf{R}) \\ \mathbf{T}_{e_t}^{o_t} &= \begin{bmatrix} e^{\mathbf{w}(1-t)} & \mathbf{v}(1-t) \\ \mathbf{0}_{1 \times 3} & 1 \end{bmatrix} \mathbf{T}_{e_1}^{o_1} \mathbf{T}_{e_t}^{e_1} = \mathbf{T}_{o_1}^{o_t} \mathbf{T}_{e_1}^{o_1} \mathbf{T}_{e_t}^{e_1}. \end{aligned} \quad (8)$$

This factorization is not only the correct way of applying the constant velocity assumption but also makes it easy to deal with the fact that, in many cases, public datasets do not release the raw \mathbf{X}_{e_t} points but instead release the ego-motion compensated points $\mathbf{T}_{e_t}^{e_1} \mathbf{X}_{e_t}$. With the above factorization, we can omit the first $\mathbf{T}_{e_t}^{e_1}$ transformation as it has already been applied. This is one of those fortunate situations where the easy and correct approaches are the same!

We can directly plug Eq. (7) and Eq. (8) into our mesh and pose steps. This is precisely what we do for the mesh step in Eq. (4), but there is one detail to account for. Point-to-surface reconstruction methods need to disambiguate between the inside and outside of the reconstructed objects. This is often done using the empty-space constraint provided by the rays connecting the sensor to each measured point. Care needs to be taken to use the continuous sensor position defined by the continuous pose, or else the reconstruction can fail.

For the pose step in Eq. (6), naively plugging it in complicates the use of off-the-shelf ICP methods. Instead, we make an approximation where we consider the intra-sweep transformations $\mathbf{T}_{e_t}^{e_1}$ and $\mathbf{T}_{o_1}^{o_t}$ to be fixed corrections applied before estimating new keyframe poses. This corresponds to the common practice of motion-compensating a sweep, but our approach produces a 360-degree sweep that is correctly compensated *for object motion* (for the first time, to our knowledge).

5 Experimental Setup

We test our method on sparse LiDAR sequences from NuScenes [3] and the Argoverse 2.0 [32]. NuScenes also has sparse annotations, providing them at 2Hz compared to measuring LiDAR sweeps at 20Hz. This sparsity allows us to showcase our method’s ability to densify in space and time. As a result, we focus our quantitative analysis on NuScenes, but similar results for Argoverse can be found in the supplemental material. NuScenes breaks the data into 20-second sequences, each containing around 400 LiDAR sweeps. Since our method does not require any training data, we focus on qualitative and quantitative evaluation of the ten validation sequences the dataset authors chose to serve as a representative sample of the data. We omit one sequence (scene-0553) since it does not contain any motion of the vehicle. For each sequence, we initialize the ego-poses using a recent LiDAR-only odometry method [28]. We initialize the object tracks and bounding boxes either by using linear interpolation on the provided object annotations or with the output of an off-the-shelf LiDAR object tracker [20]. We then run 100 iterations of refinement on all of the objects and

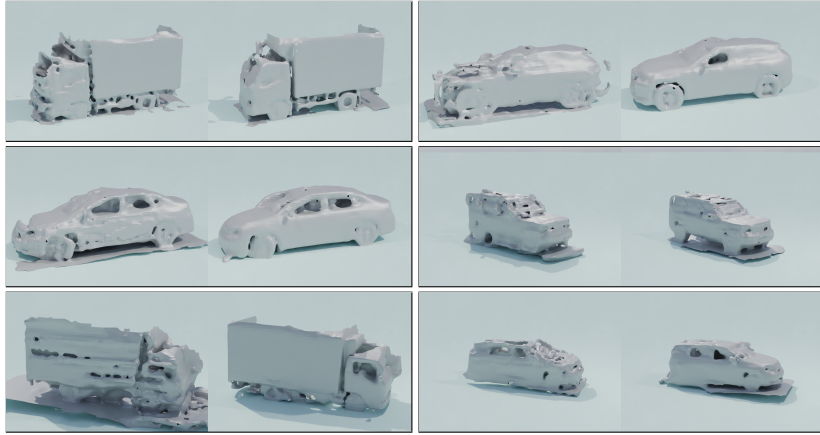


Fig. 7: (Left) Each column shows NuScenes and Argoverse object reconstructions using ground truth poses compared to (right) ours.

background maps, with early stopping criteria to avoid wasted computation. Iterations are stopped if the mean registration error for an object falls below 1 centimeter for three consecutive iterations. For the mesh step, we use the default parameters of the publicly released Neural Kernel Surface Reconstruction model [10]. For the pose update, once we have deskewed the dynamic objects, we use a standard ICP implementation [39] with a point-to-plane loss, a robust Huber kernel with $k = 0.2$ and a matching threshold of 1.5 meters.

For the tracking results, we use the Centerpoint-based [36] object detector LT3D [20] to extract bounding boxes in all frames. We then use greedy association to turn the detections into object tracks.

6 Qualitative Results

Visualizations of our foreground reconstructions on NuScenes and Argoverse are shown in Fig. 7. In the visualizations, we show that the ground-truth object annotations are not accurate enough to yield good reconstruction. Errors in bounding box alignment and orientation lead to point aggregation errors, leading to poor surface reconstructions. The fact that our refined object poses lead to better reconstructions is evidence that we produce better annotations than the ground truth. Motion distortion from dynamic objects also contributes to the poor quality of the ground truth reconstructions. In figure 2, we show how accounting for this distortion can significantly improve the reconstructions.

Background reconstructions from NuScenes are shown in Fig. 9 and Argoverse in Fig. 8. For these “objects” the quality improvement comes from refining the ego-pose of the vehicle. As with foreground objects, ego-pose errors cause misalignment of the LiDAR sweeps, which become surface artifacts. However, the comparison is with a state-of-the-art LiDAR odometry method instead of the ground truth. We use odometry because it performs better than the ground-truth ego-poses.

	NN Dist (m) ↓	Acc Relax ↑	Acc Strict ↑
DSNerf [5]	0.537	0.81	0.70
SUDS [25]	0.18	0.94	0.88
NKSR [10] + GT tracks (2Hz)	0.071	0.9	0.76
NKSR [10] + LT3D [20] tracks (2Hz)	0.071	0.9	0.76
Ours + GT tracks (2 Hz)	0.048	0.96	0.91
Ours + GT tracks (1 Hz)	0.050	0.96	0.90
Ours + GT tracks (0.5 Hz)	0.048	0.96	0.91
Ours + GT tracks (0.25 Hz)	0.048	0.96	0.91
Ours + LT3D [20] tracks	0.048	0.96	0.90

Table 1: Surface quality evaluation on NuScenes, measured by comparing the LiDAR points to their closest points on the reconstructed surfaces.

7 Quantitative Results

We analyze how well our piecewise rigid model can represent the dynamic scenes. Recent works that use volumetric scene representations [5, 25] typically use ray-casting along the ground-truth ray directions to measure this property. However, we find that this metric is dominated by large outlier errors caused by rays missing an object boundary. This makes the metric hard to interpret since it is a mixture of two different error distributions. Instead, we propose to measure reconstruction accuracy using the nearest-neighbor distance between the input point clouds and the reconstructed scene at each timestamp. We report the average distance and two accuracy metrics to characterize the distribution of errors. Specifically, we compute the percent of points less than 10cm and 5cm for the relaxed and strict metrics, respectively.

We compare our method using different inputs (ground truth annotations with varying rates of subsampling and the output of an object tracker) to several strong baselines. First, we compare with DS-Nerf [5] and SUDS [25], two NeRF-style [16] models which have been adapted to urban scenes with LiDAR inputs. Second, we compare with the surface reconstruction method NKSR [10] combined with either ground truth object tracking or the results of the off-the-shelf tracker we use.

As seen in Tab. 1, our method outperforms all baselines. We find that the NeRF style methods are good at reconstructing most points, leading to high accuracy metrics, but are prone to significant outlier errors, leading to poor average error. On the other hand, the surface-based method achieves better average error but fails at reconstructing fine detail, leading to low strict accuracy. In contrast, our method produces suitable high-level geometry, leading to low average error, and faithfully reconstructs fine details, leading to high accuracy.

We use the same annotation subsampling technique to evaluate the improvement of our estimates of the locations of the dynamic objects in the scenes. By omitting input annotations, we can compare our method’s predicted object locations to the ground truth using the NuScenes’ Average Translation Error metric [3]. We compute this metric over the nine test sequences and filter out

	ATE (m) ↓		
	1Hz	0.5Hz	0.25Hz
Interpolation	0.29	0.40	0.74
Ours	0.20	0.22	0.52

Table 2: Pose accuracy evaluation on NuScenes (using NuScene’s default ATE metric), measured by comparing the bounding box locations predicted by our method to held-out ground truth labels provided at 2Hz. We compare our method to linearly interpolating the poses as is commonly done to create scene-flow labels [1].

objects that follow linear trajectories. As shown in Tab. 2, our method improves the estimates of complex object motions.

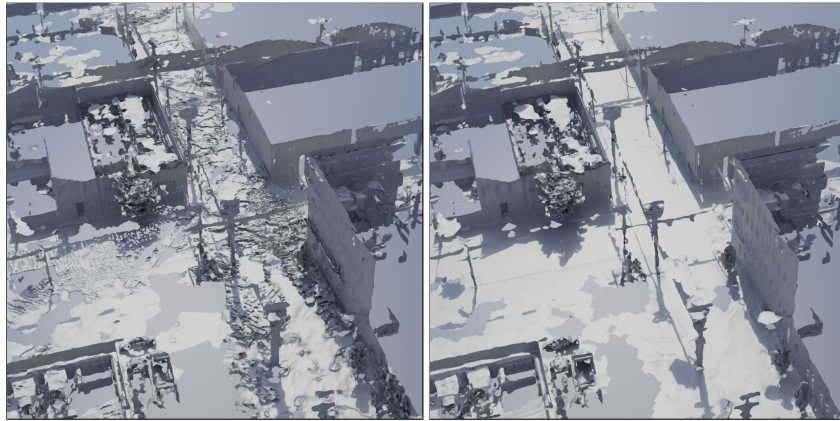


Fig. 8: (Left) Map reconstruction on Argoverse 2.0 using *ground truth* poses compared to (right) ours.

8 Conclusion

In this work, we brought dense, dynamic reconstruction to the large-scale in-the-wild autonomous vehicle setting. We developed an optimization framework for understanding this problem and provided a simple yet effective solution based on decomposing the problem into well-studied sub-components. This solution yields high-quality reconstructions of both the foreground and background and can even account for subtle distortions in the input point clouds. We hope that this method will not only be useful for creating training and evaluation data for other perception tasks but will also promote active research in this challenging setting.

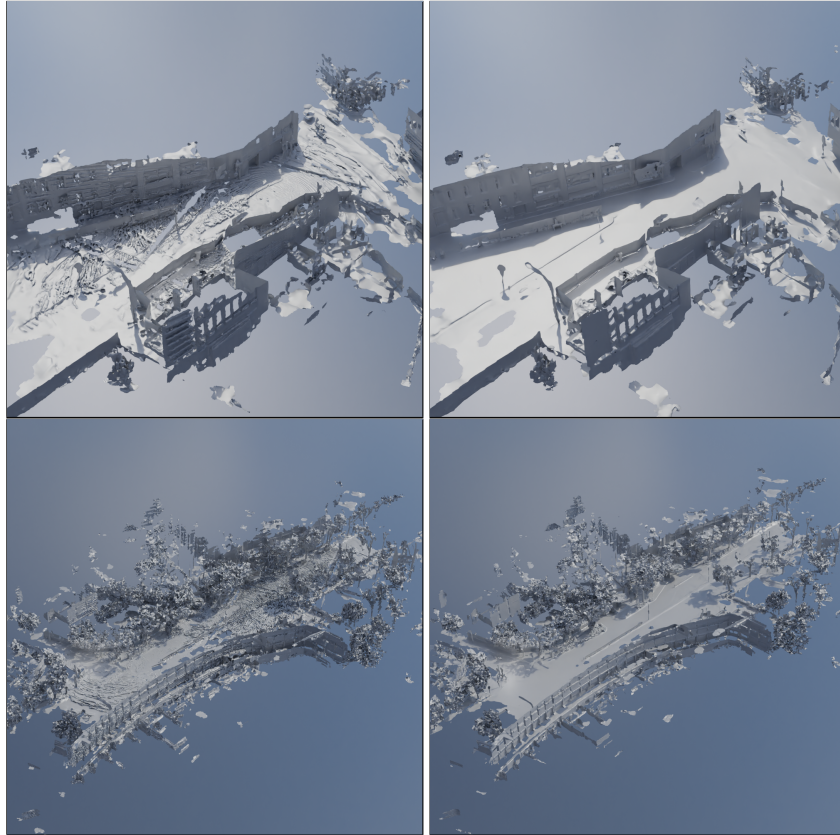


Fig. 9: (Left) Map reconstructions using odometry poses compared to (right) ours. Ground-truth ego poses produce even worse results since NuScenes does not align poses in the z (height) dimension.

References

1. Baur, S.A., Emmerichs, D.J., Moosmann, F., Pinggera, P., Ommer, B., Geiger, A.: Slim: Self-supervised lidar scene flow and motion segmentation. In: ICCV. pp. 13126–13136 (2021) [3](#), [13](#)
2. Bibby, C., Reid, I.: Simultaneous localisation and mapping in dynamic environments (slamde) with reversible data association. In: Proceedings of Robotics: Science and Systems. vol. 66, p. 81 (2007) [4](#)
3. Caesar, H., Bankiti, V., Lang, A.H., Vora, S., Liong, V.E., Xu, Q., Krishnan, A., Pan, Y., Baldan, G., Beijbom, O.: nuscenes: A multimodal dataset for autonomous driving. In: Proceedings of the IEEE/CVF conference on computer vision and pattern recognition. pp. 11621–11631 (2020) [2](#), [10](#), [12](#)
4. Chodosh, N., Simon, L., Deva, R.: Re-evaluating lidar scene flow (2024) [1](#), [3](#)
5. Deng, K., Liu, A., Zhu, J.Y., Ramanan, D.: Depth-supervised nerf: Fewer views and faster training for free. In: Proceedings of the IEEE/CVF Conference on Computer Vision and Pattern Recognition. pp. 12882–12891 (2022) [12](#)
6. Dewan, A., Caselitz, T., Tipaldi, G.D., Burgard, W.: Motion-based detection and tracking in 3d lidar scans. In: 2016 IEEE international conference on robotics and automation (ICRA). pp. 4508–4513. IEEE (2016) [4](#)
7. Gojcic, Z., Litany, O., Wieser, A., Guibas, L.J., Birdal, T.: Weakly supervised learning of rigid 3d scene flow. In: Proceedings of the IEEE/CVF conference on computer vision and pattern recognition. pp. 5692–5703 (2021) [1](#)
8. Hähnel, D., Schulz, D., Burgard, W.: Map building with mobile robots in populated environments. In: IROS. pp. 496–501 (2002) [4](#)
9. Henein, M., Zhang, J., Mahony, R., Ila, V.: Dynamic slam: The need for speed. In: 2020 IEEE International Conference on Robotics and Automation (ICRA). pp. 2123–2129. IEEE (2020) [4](#)
10. Huang, J., Gojcic, Z., Atzmon, M., Litany, O., Fidler, S., Williams, F.: Neural kernel surface reconstruction. In: Proceedings of the IEEE/CVF Conference on Computer Vision and Pattern Recognition. pp. 4369–4379 (2023) [7](#), [11](#), [12](#), [19](#)
11. Jiang, C., Fougerolle, Y., Fofi, D., Demonceaux, C.: Dynamic 3d scene reconstruction and enhancement. In: Image Analysis and Processing-ICIAP 2017: 19th International Conference, Catania, Italy, September 11–15, 2017, Proceedings, Part I 19. pp. 518–529. Springer (2017) [4](#)
12. Kazhdan, M., Bolitho, M., Hoppe, H.: Poisson surface reconstruction. In: Proceedings of the fourth Eurographics symposium on Geometry processing. vol. 7, p. 0 (2006) [7](#)
13. Li, H., Yu, J., Ye, Y., Bregler, C.: Realtime facial animation with on-the-fly correctives. ACM Trans. Graph. **32**(4), 42–1 (2013) [4](#)
14. Li, X., Kaesemodel Pontes, J., Lucey, S.: Neural scene flow prior. NeurIPS **34**, 7838–7851 (2021) [3](#)
15. Manivasagam, S., Wang, S., Wong, K., Zeng, W., Sazanovich, M., Tan, S., Yang, B., Ma, W.C., Urtasun, R.: Lidarsim: Realistic lidar simulation by leveraging the real world. In: Proceedings of the IEEE/CVF Conference on Computer Vision and Pattern Recognition. pp. 11167–11176 (2020) [4](#)
16. Mildenhall, B., Srinivasan, P.P., Tancik, M., Barron, J.T., Ramamoorthi, R., Ng, R.: Nerf: Representing scenes as neural radiance fields for view synthesis. Communications of the ACM **65**(1), 99–106 (2021) [12](#)
17. Mitra, N.J., Flöry, S., Ovsjanikov, M., Gelfand, N., Guibas, L.J., Pottmann, H.: Dynamic geometry registration. In: Symposium on geometry processing. pp. 173–182 (2007) [3](#)

18. Newcombe, R.A., Fox, D., Seitz, S.M.: Dynamicfusion: Reconstruction and tracking of non-rigid scenes in real-time. In: Proceedings of the IEEE conference on computer vision and pattern recognition. pp. 343–352 (2015) [1](#), [4](#)
19. Palafox, P., Božič, A., Thies, J., Nießner, M., Dai, A.: Npms: Neural parametric models for 3d deformable shapes. In: Proceedings of the IEEE/CVF International Conference on Computer Vision. pp. 12695–12705 (2021) [4](#)
20. Peri, N., Dave, A., Ramanan, D., Kong, S.: Towards long-tailed 3d detection. In: Conference on Robot Learning. pp. 1904–1915. PMLR (2023) [10](#), [11](#), [12](#), [19](#)
21. Qian, C., Sun, X., Wei, Y., Tang, X., Sun, J.: Realtime and robust hand tracking from depth. In: Proceedings of the IEEE conference on computer vision and pattern recognition. pp. 1106–1113 (2014) [4](#)
22. Runz, M., Buffier, M., Agapito, L.: Maskfusion: Real-time recognition, tracking and reconstruction of multiple moving objects. In: 2018 IEEE International Symposium on Mixed and Augmented Reality (ISMAR). pp. 10–20. IEEE (2018) [1](#)
23. Taylor, J., Shotton, J., Sharp, T., Fitzgibbon, A.: The vitruvian manifold: Inferring dense correspondences for one-shot human pose estimation. In: 2012 IEEE Conference on Computer Vision and Pattern Recognition. pp. 103–110. IEEE (2012) [4](#)
24. Tian, R., Zhang, Y., Cao, Z., Zhang, J., Yang, L., Coleman, S., Kerr, D., Li, K.: Object slam with robust quadric initialization and mapping for dynamic outdoors. IEEE Transactions on Intelligent Transportation Systems (2023) [4](#)
25. Turki, H., Zhang, J.Y., Ferroni, F., Ramanan, D.: Suds: Scalable urban dynamic scenes. In: Proceedings of the IEEE/CVF Conference on Computer Vision and Pattern Recognition. pp. 12375–12385 (2023) [12](#), [18](#), [19](#)
26. Uhrig, J., Schneider, N., Schneider, L., Franke, U., Brox, T., Geiger, A.: Sparsity invariant cnns. In: 2017 international conference on 3D Vision (3DV). pp. 11–20. IEEE (2017) [3](#)
27. Vizzo, I., Chen, X., Chebrolu, N., Behley, J., Stachniss, C.: Poisson surface reconstruction for lidar odometry and mapping. In: 2021 IEEE International Conference on Robotics and Automation (ICRA). pp. 5624–5630. IEEE (2021) [4](#)
28. Vizzo, I., Guadagnino, T., Mersch, B., Wiesmann, L., Behley, J., Stachniss, C.: KISS-ICP: In Defense of Point-to-Point ICP – Simple, Accurate, and Robust Registration If Done the Right Way **8**(2), 1–8 (2023). <https://doi.org/10.1109/LRA.2023.3236571> [10](#), [19](#)
29. Wang, C.C., Thorpe, C., Thrun, S., Hebert, M., Durrant-Whyte, H.: Simultaneous localization, mapping and moving object tracking. The International Journal of Robotics Research **26**(9), 889–916 (2007) [4](#)
30. Wang, J., Manivasagam, S., Chen, Y., Yang, Z., Bârsan, I.A., Yang, A.J., Ma, W.C., Urtasun, R.: Cadsim: Robust and scalable in-the-wild 3d reconstruction for controllable sensor simulation. In: Conference on Robot Learning. pp. 630–642. PMLR (2023) [4](#)
31. Wang, Y., Dai, Y., Liu, Q., Yang, P., Sun, J., Li, B.: Cu-net: Lidar depth-only completion with coupled u-net. IEEE Robotics and Automation Letters **7**(4), 11476–11483 (2022) [3](#)
32. Wilson, B., Qi, W., Agarwal, T., Lambert, J., Singh, J., Khandelwal, S., Pan, B., Kumar, R., Hartnett, A., Pontes, J.K., Ramanan, D., Carr, P., Hays, J.: Argoverse 2: Next generation datasets for self-driving perception and forecasting. In: Proceedings of the Neural Information Processing Systems Track on Datasets and Benchmarks (NeurIPS Datasets and Benchmarks 2021) (2021) [2](#), [10](#)

33. Yang, G., Vo, M., Neverova, N., Ramanan, D., Vedaldi, A., Joo, H.: Banmo: Building animatable 3d neural models from many casual videos. In: Proceedings of the IEEE/CVF Conference on Computer Vision and Pattern Recognition. pp. 2863–2873 (2022) [1](#)
34. Yang, S., Scherer, S.: Cubeslam: Monocular 3-d object slam. *IEEE Transactions on Robotics* **35**(4), 925–938 (2019) [4](#)
35. Yang, Z., Manivasagam, S., Chen, Y., Wang, J., Hu, R., Urtasun, R.: Reconstructing objects in-the-wild for realistic sensor simulation [4](#)
36. Yin, T., Zhou, X., Krahenbuhl, P.: Center-based 3d object detection and tracking. In: Proceedings of the IEEE/CVF conference on computer vision and pattern recognition. pp. 11784–11793 (2021) [11](#)
37. Yu, T., Zheng, Z., Guo, K., Liu, P., Dai, Q., Liu, Y.: Function4d: Real-time human volumetric capture from very sparse consumer rgbd sensors. In: Proceedings of the IEEE/CVF conference on computer vision and pattern recognition. pp. 5746–5756 (2021) [1](#)
38. Zhao, Y., Bai, L., Zhang, Z., Huang, X.: A surface geometry model for lidar depth completion. *IEEE Robotics and Automation Letters* **6**(3), 4457–4464 (2021) [3](#)
39. Zhou, Q.Y., Park, J., Koltun, V.: Open3D: A modern library for 3D data processing. arXiv:1801.09847 (2018) [11](#)

9 Bounding Box Evaluation Details

We used the standard NuScenes object detection metric, average translation error, to measure our method’s improvement of the ground-truth bounding boxes. However, as our method is not an object detector, that comparison has some complications, which we explain here.

The average translation error is defined as the distance between the centers of the predicted and ground truth bounding boxes. Since our method does not predict bounding boxes, first, we need to define a “center” for them. The center has no meaning for our reconstruction, so we can choose any fixed point on each object. Specifically, we choose the point that minimizes the sum of square distances to the centers of all the input bounding boxes. Note that when we sub-sample the inputs for evaluation, we do not use the held-out boxes to determine the “predicted center”.

Next, we must define what constitutes a “detection” for our algorithm. Our reconstructions are formed by aggregating many points over multiple sweeps, which are registered to the predicted surfaces. Due to the labeling procedure of NuScenes, some of these input bounding boxes contain very few LiDAR returns (< 50). The lack of points causes ambiguities in the registration step and can lead to instabilities, so we drop them from the optimization. In table Tab. 2, we show the results on only boxes that have been optimized by our method.

10 Surface Quality Evaluation Details

To evaluate NeRF-style models using the nearest neighbor distance, we need to convert their volumetric representations into some kind of geometric primitive. For static scenes NeRF models can be converted into mesh but this is not as well defined for dynamic models such as SUDS [25]. Since these models use depth supervision by projecting the point clouds into the RGB image planes, we use the depth estimations from these frames to evaluate the reconstruction accuracy.

For each test frame we use the estimated dense depth to create a point cloud. We then compute the nearest-neighbors between the ground truth points which were projected into that frame and that point cloud. This evaluation protocol has the advantage that it can be applied to any method (dynamic or static) that can produce depth map estimates and avoids any post-processing to extract a mesh that the method might not have been designed for.

11 Argoverse 2.0 Evaluation

We replicated the same evaluation as done on NuScenes on Argoverse 2.0. As with NuScenes we use a small subset of the validation dataset for our evaluation. Specifically, sequences: a7636fca-4d9e-3052-bef2-af0ce5d1df74, 0c3bad78-9f1e-395d-a376-2eb7499229fd, e50e7698-de3d-355f-aca2-eddd09c09533, 0aa4e8f5-2f9a-39a1-8f80-c2fdde4405a2 d770f926-bca8-31de-9790-73fbb7b6a890.

	NN Dist (m) ↓	Acc Relax ↑	Acc Strict ↑
SUDS [25]	0.70	0.93	0.87
NKSR [10] + GT tracks (10Hz) + GT ego-pose	0.086	0.89	0.76
NKSR [10] + LT3D [20] tracks + GT ego-pose	0.088	0.89	0.73
Ours + GT tracks (10 Hz) + KISS ego-pose [28]	0.074	0.93	0.82
Ours + GT tracks (10 Hz) + GT ego-pose	0.079	0.93	0.81
Ours + GT tracks (5 Hz) + GT ego-pose	0.073	0.93	0.83
Ours + GT tracks (2.5 Hz) + GT ego-pose	0.073	0.93	0.83
Ours + LT3D [20] tracks + GT ego-pose	0.083	0.92	0.79

Table 3: Surface quality evaluation on Argoverse 2.0, measured by comparing the LiDAR points to their closest points on the reconstructed surfaces.

As with NuScenes, we tested our method with various modifications to the inputs, either downsampling the ground truth annotations or by using tracked produced by LT3d [20]. The results can be found in tables Tab. 3 and reconfirm our main findings in the NuScenes results: our method can produce high-quality reconstructions even with input annotations of significantly worse quality than the ground truth. Again, we also see a large improvement over simply running a point-to-surface method (NKSR) over points aggregated using ground truth labels and poses. The NeRF-based approach SURF also suffers from the same problem as was found in NuScenes: large outlier errors resulting in very high average error.

12 Failure Cases

Ground Holes in AV2 Background Reconstructions: We find (and show in Fig. 8) that the ground surface we extract from Argoverse is not as complete as those we extract from NuScenes. We believe that this is the result of the orientation of the LiDAR lasers used in each dataset collection. The LiDAR lasers in AV2 are oriented such that they focus the resolution "down-range" to make detecting vehicles and pedestrians easier. This results in less resolution on the ground. To see this, compare the distance between laser returns near the car in NuScenes and Argoverse in Fig. 6. Despite this, we still believe that good reconstructions of the ground should be possible and investigating this is an area of future research.

Registration Failures: Another source of errors for our method is when ICP produces a poor registration on a vehicle. One common cause of this is attempting to register a sweep to a vehicle that contains very few points. We use a heuristic to filter out most of these cases (dropping views of an object with fewer than 50 points) but some can still cause errors which manifest as "jittery" motion of objects. Another, harder to filter, source of error is from registering scans with low "texture". In the context of ICP, low texture means scans which do not contain corners or edges useful for exact alignment. This can occur when only the side face of a vehicle is observed, resulting in a flat plane of points which has many possible alignments to the reconstructed shape. We believe that both of these errors can be mitigated by applying stronger motion priors to the reconstructed objects in order to add constraints to the system. This is another direction for future work.